ADVANCED FUNCTIONAL MATERIALS
www.afm-journal.de

Synergistic Active Phases of Transition Metal Oxide Heterostructures for Highly Efficient Ammonia Electrosynthesis

Di Yin, Dong Chen, Yuxuan Zhang, Weijun Wang, Quan Quan, Wei Wang, You Meng, Zhengxun Lai, Zhe Yang, SenPo Yip, Chun-Yuen Wong, Xiuming Bu,* Xianying Wang, and Johnny C. Ho**

Electrochemically converting waste nitrate (NO_3^-) into ammonia (NH_3) is a green route for both wastewater treatment and high-value-added ammonia generation. However, the NO_3^--to-NH_3 reaction involves multistep electron transfer and complex intermediates, making it a grand challenge to drive efficient NO_3^- electroreduction with high NH_3 selectivity. Herein, an in-operando electrochemically synthesized Cu_2O/NiO heterostructure electrocatalyst is proven for efficient NH_3 electrosynthesis. In situ Raman spectroscopy reveals that the obtained Cu_2O/NiO, induced by the electrochemistry-driven phase conversion, is the real active phase. This electronically coupled phase can modulate the interfacial charge distribution, dramatically lower the overpotential in the rate-determining step and thus requiring lower energy input to proceed with the NH_3 electrosynthesis. The orbital hybridization calculations further identify that Cu_2O is beneficial for NO_3^- adsorption, and NiO could promote the desorption of NH_3, forming an excellent tandem electrocatalyst. Such a tandem system leads to NH_3 Faradaic efficiency of 95.6%, a super-high NH_3 selectivity of 88.5% at −0.2 V versus RHE, surpassing most of the NH_3 electrosynthesis catalysts at an ultralow reaction voltage.

1. Introduction

Ammonia (NH_3), a versatile raw ingredient (industrial chemical), can be used as a feedstock to synthesize fertilizers, dyes, pharmaceuticals, etc.[1] Currently, the main synthetic route for NH_3 is the Haber–Bosch process, which requires harsh reaction conditions and ultrahigh energy consumption and releases large amounts of CO_2.[2,3] Meanwhile, large-scale industrial nitrogen fixation also leads to the most extensive disturbance of the nitrogen cycle. Nowadays, electrochemical nitrogen (N_2) reduction reaction (NRR) has been widely considered as a sustainable approach for preparing green ammonia via atmospheric nitrogen and water under mild conditions.[4] However, the large bond energy of the N≡N triple bond (941 kJ mol^{-1}), limited N_2 solubility, and competing hydrogen evolution reaction lead to the low reaction rate, selectivity, and Faradic efficiency (FE) of NRR.[5,6] In contrast, nitrate-rich wastewater as an attractive nitrogen source for ammonia electrosynthesis (nitrate reduction reaction, NO_3^-RR) is energy-efficient (204 kJ mol^{-1}) and contributes to restoring the global imbalance nitrogen cycle.[7]

Since NO_3^-RR ($NO_3^- + 6H_2O + 8e^- \rightarrow NH_3 + 9OH^-$, $E^0 = 0.69$ V vs RHE) involves eight electrons transfer coupled with nine OH^- generation processes and thus suffers from various byproducts (i.e., NO_2^-, N_2).[8–10] To this end, electrocatalysts with higher efficiency and selectivity are required to utilize nitrate to produce value-added NH_3 selectively. In recent years, copper-based catalysts have been intensively investigated due to their favorable nitrate

D. Yin, D. Chen, Y. Zhang, W. Wang, Q. Quan, W. Wang, Y. Meng, Z. Lai, J. C. Ho
Department of Materials Science and Engineering
City University of Hong Kong
Kowloon, Hong Kong SAR 999077, P. R. China
E-mail: johnnyho@cityu.edu.hk

W. Wang, Y. Meng, J. C. Ho
State Key Laboratory of Terahertz and Millimeter Waves
City University of Hong Kong
Kowloon, Hong Kong SAR 999077, P. R. China

Z. Yang, C.-Y. Wong
Department of Chemistry
City University of Hong Kong
Kowloon, Hong Kong SAR 999077, P. R. China
E-mail: acywong@cityu.edu.hk

S. Yip, J. C. Ho
Institute for Materials Chemistry and Engineering
Kyushu University
Fukuoka 816-8580, Japan

X. Bu, X. Wang
Energy Materials Research Center AG Hydrogen Materials & Devices
CAS Key Laboratory of Materials for Energy Conversion
Shanghai Institute of Ceramics
Chinese Academy of Sciences
Shanghai 200050, P. R. China
E-mail: xiumingbu2-c@my.cityu.edu.hk

The ORCID identification number(s) for the author(s) of this article can be found under https://doi.org/10.1002/adfm.202303803

DOI: 10.1002/adfm.202303803

binding ability and poor H intermediate binding ability.[11–13] However, the fabricated copper-based catalyst is prone to suffer from complex surface reconstruction processes during the reduction environment in the forms of valence variations, anion/cation defects generations, phase transformation/separation, etc.[14,15] In particular, recent works demonstrated Cu-based catalysts experienced the potential-dependent transformation from bivalent copper to monovalent copper, in which the existence of univalent copper is beneficial to inhibit hydrogen generation and regulate the Gibbs free energy of NO_3^-RR intermediates.[16–18] It is worth noting that the active intermediate state of monovalent copper is unstable and can be rapidly reduced to metallic copper under high reduction potential (< −0.5 V vs RHE), resulting in a large number of absorbed intermediates (e.g., NO_2^- and NO) passivated surface, which not only leads to the reduction of catalytic activity but also causes great troubles for the rational design and mechanism analysis of the catalyst. In addition, inspired by the tandem NO_3^- to NH_3 conversion in nature, multi-phase interactions may circumvent the scaling relations to achieve ammonia production.[19,20] Even though the Cu alloying strategy (e.g., CuRh,[21] CuNi,[22,23] and CuPd,[24,25] etc.) can achieve excellent FE (more than 80%) and ammonia selectivity (more than 70%), the overpotential is still greater than −0.5 V because of the linear scaling relationships (LSR).[26,27] Such a high overpotential is detrimental to the survival of the real active sites and increases energy consumption.[18,28] Therefore, it is important to stabilize the real active sites of the catalyst with a low applied overpotential, which is vital for guiding the rational design and mechanism analysis of certain catalytic materials for NO_3^-RR.

Herein, we report the in situ electrochemistry-driven phase conversion strategy to reconstruct and stabilize the active Cu_2O/NiO intermediate phase via a binary metal oxide CuO/NiO. In situ Raman spectra, Auger spectra, and high-resolution transmission electron microscopy (HRTEM) characterizations revealed that the Cu_2O/NiO active phase was reconstructed and stabilized at low overpotentials during the whole NO_3^-RR process. Density functional theory (DFT) calculations exhibit that the Cu_2O/NiO interface is the optimal active site for NO_3^-RR due to the electron-coupled interactions between Cu_2O and NiO. Those two active phases can also be combined into a tandem system to break the adsorption–energy scaling relationship, which exhibits strong NO_3^- adsorption at Cu_2O and rapid NH_3 release at NiO. As a result, the intermediate active phase of Cu_2O/NiO reveals a superior electrocatalytic NO_3^--to-NH_3 activity at −0.2 V versus RHE with a FE of 95.6%, a high NH_3 selectivity of 88.5% and the ammonia-evolving rate of 2.1 mol h^{-1} m^{-2}, surpassing most of the NO_3^-RR catalysts at an ultralow reaction voltage.

2. Results and Discussion

The fabrication of CuO/NiO heterostructures on Ni foam is illustrated in **Figure 1**a. First, the Cu-doped Ni foam (NF) was synthesized via a galvanic displacement reaction. The CuO/NiO heterostructures on NF were then obtained through annealing in the air (a detailed fabrication process was shown in the Experimental Section). Comparing the XRD patterns of Cu-doped NF and pristine NF, the diffraction peaks exhibit a slight shift after galvanic displacement, confirming that Cu atoms successfully substitute Ni counterparts (Figure S1, Supporting Information). During synthesis, an obvious color change in NF from silver to black was observed after the annealing treatment (Figure S2, Supporting Information). Based on the scanning electron microscopy (SEM) characterizations, the CuO/NiO layer with an average thickness of ≈100 nm could be in situ formed on the nickel substrate (Figure 1b,c). Meanwhile, the framework of NF could be well preserved to achieve sufficient electrochemically active surface area for enhanced NO_3^-RR performance (Figure S3, Supporting Information). The morphology of CuO/NiO heterostructure was also characterized by the HRTEM and the corresponding selected area electron diffraction (SAED) (Figure 1d,e). The well-defined CuO phase with an interplanar spacing of 0.232 nm for the (111) plane is closely connected with the (200) and (111) facets of NiO with the lattice fringes distances of 0.209 and 0.241 nm, respectively. The concrete phase will be indicated in subsequent XRD tests. Clear boundaries could as well be observed between CuO and NiO phases. In addition, the SAED pattern shows the diffraction rings with the random arrangement of bright spots, matching well with the (111) and (40-2) planes of CuO and the (111) and (220) planes of NiO.[29,27] The element mapping presents the uniform distribution of Cu and Ni on the electrocatalyst surface, indicating the successful formation of the CuO/NiO tandem catalyst (Figure 1f–i).

To describe the formation of CuO/NiO heterostructures, a series of temperature-controlled catalysts were synthesized at 300, 400, 500, and 600 °C. The cross-sectional SEM images depicted that the thicknesses of in situ formed layers increased along with the raised temperature (Figure S4, Supporting Information). Raman spectra of CuO/NiO heterostructures synthesized at different temperatures are displayed in **Figure 2**a. CuO obtained at 300 °C and the bands indexed at 281, 330, and 605 cm^{-1} were assigned to the Ag, Bg′, and Bg′′ modes of CuO, which confirms the formation of single phase and highly crystalline CuO structures at the low temperature. The longitudinal optical (LO) of NiO (Ni^{II}–O) at 510 cm^{-1} could also be observed when increasing the temperature up to 400 °C.[30] As the calcination temperature further increases, Ni^{III}–O vibrations appear at 475 and 550 cm^{-1}.[31] XRD patterns were as well collected to further reveal the synthetic process of CuO/NiO heterostructures (Figure 2b). The sample synthesized at 300 °C showed several diffraction peaks at 35.42°, 38.71°, 44.51°, 51.85°, 76.37°, and 86.53°, corresponding to (002), (111), (40-2) lattice planes of CuO (JCPDS no. 48-1548) and (111), (200), (220) lattice planes of Ni (JCPDS no. 04-0850), respectively.[32] Since the penetration depth of XRD is larger than the total thickness of the CuO/NiO layer, the diffracting peaks of the nickel foam substrate could also be observed. Apart from the diffraction patterns of CuO and Ni, the diffraction patterns of the sample synthesized at 400 °C demonstrated the formation of fcc-structured NiO as evidenced by the (111) and (200) planes, respectively, at 37.2° and 43.3° (JCPDS no. 71-1179).

To shed light on the electron distribution at the interface of CuO/NiO heterostructures, the band structures, chemical states, and electronic interactions were thoroughly investigated. First, the ultraviolet photoelectron spectroscopy (UPS) measurements were performed to ascertain the work functions (Φ) and the valence band maximum (E_V) of CuO, NiO, and CuO/NiO heterostructures (Figure S5, Supporting Information). The work function of CuO was calculated to be 4.41 eV, which is larger

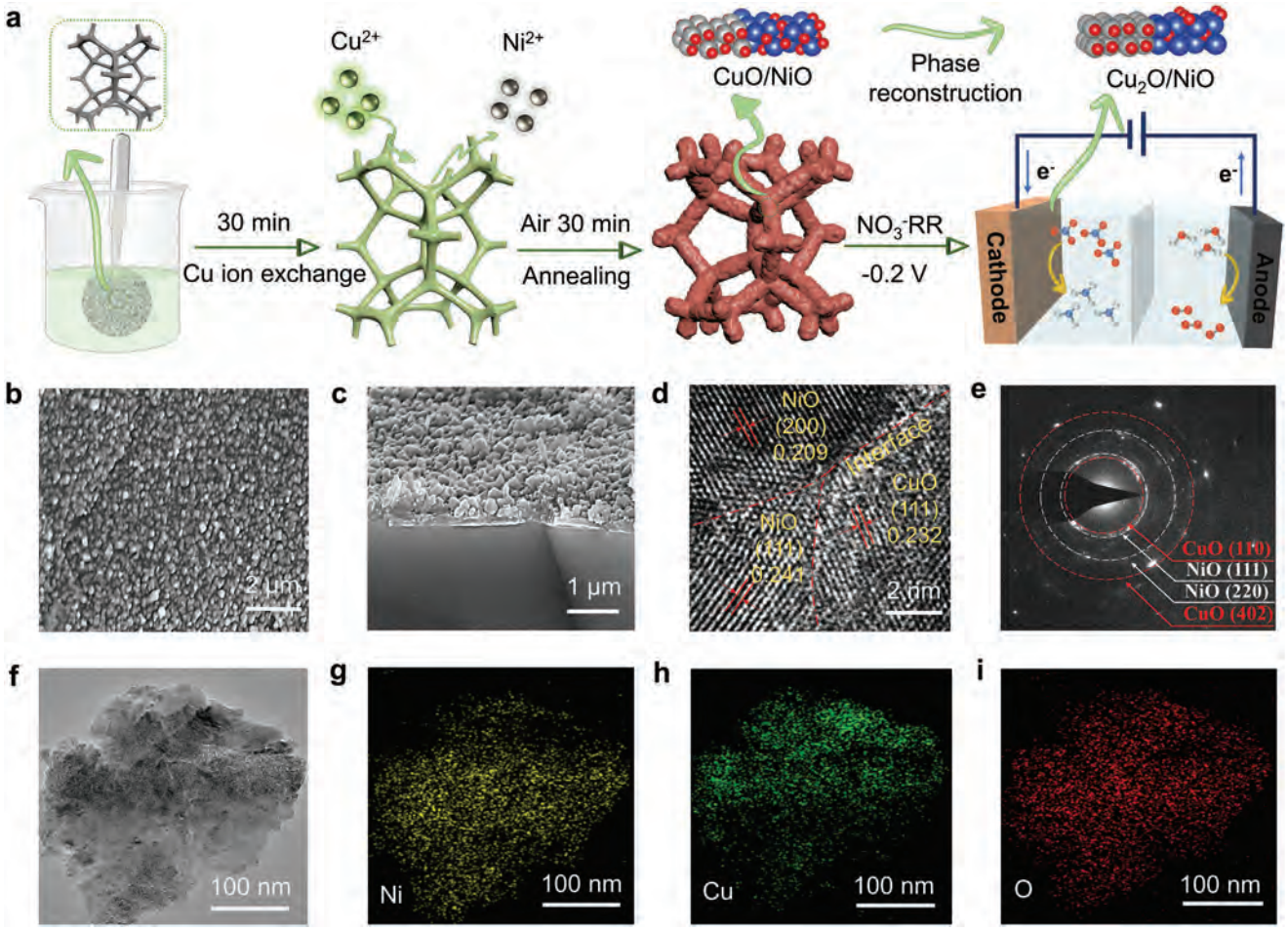

Figure 1. Synthesis and morphology of the CuO/NiO heterostructure. a) Schematic illustration of the synthesis of CuO/NiO and its phase transformation. b,c) Surficial and cross-sectional field-emission scanning electron microscope images of CuO/NiO. d) HRTEM and e) SAED pattern of CuO/NiO, where different component crystalline phases are marked out. f–i) HRTEM and the corresponding HRTEM-EDS elemental mapping images of CuO/NiO.

than that of NiO (4.16 eV), as presented in Figure S5a,b (Supporting Information). Hence, the Fermi level (E_F) versus the vacuum level of CuO was calculated to be −4.41 eV, below that of NiO (−4.16 eV). Next, the E_V position of CuO and NiO are found to be located at −4.58 and −4.61 eV, accordingly (inset in Figure S5a,b, Supporting Information). Then, the conduction band edge energy (E_C) positions of CuO and NiO are determined to be −2.71 and −0.66 eV. Thus, the energy band structures of the CuO–NiO p–p heterojunctions could be compiled and depicted in Figure 2c.[33] Because the position of the Fermi level of NiO is higher than that of CuO, electrons will flow from NiO to CuO until a Fermi equilibrium state. The electron flow leads to the opposite space–charge region at the CuO/NiO heterostructure interface and further generates the built-in electric field. The strongly coupled heterointerfaces with built-in electric fields can facilitate interfacial charge migration and accelerate NO_3^-RR reaction kinetics.[33] The element valence states of CuO/NiO heterostructures were further elucidated by X-ray photoelectron spectroscopy (XPS) (Figure 2d,e). The Cu 2p3/2, Cu 2p1/2 peaks and the related satellite peaks of CuO and CuO/NiO could be ascribed to CuO species. It is worthwhile to point out that those characteristic Cu^{2+} peaks of the CuO/NiO composites shift to low binding energy compared with those of CuO. The core-level Ni 2p spectrum in NiO and CuO/NiO exhibit the characteristic Ni 2p3/2, Ni 2p1/2 peaks and the related satellite peaks, indicating the presence of Ni^{2+} with small amounts of Ni^{3+}.[34] The Ni 2p peaks of CuO/NiO composites present a slight positive shift compared with those of bare NiO components. Those slight shifts provide important evidence for successfully constructing the electronic coupled interface between CuO and NiO, which leads to charge transfer from NiO to CuO. This electron movement tendency is consistent with the UPS analysis mentioned above. To obtain further insights, density functional theory (DFT) calculations were employed to analyze the electronic distribution of CuO/NiO heterostructures.[35–37] In this case, the charge density map of CuO/NiO heterostructure was calculated (Figure 2f). The yellow and indigo-blue regions represent the accumulation and depletion of charge density, respectively. Apparently, the interface of CuO/NiO gathers with large electron clouds, which implies the formation of a built-in electric field at the interface, leading to the continuous electron flow between two active phases.[38] Thus, the interface region of the CuO/NiO heterostructure will be the optimal adsorbed site for intermediate species. The electronic modulation of the CuO/NiO is also reflected by the changed

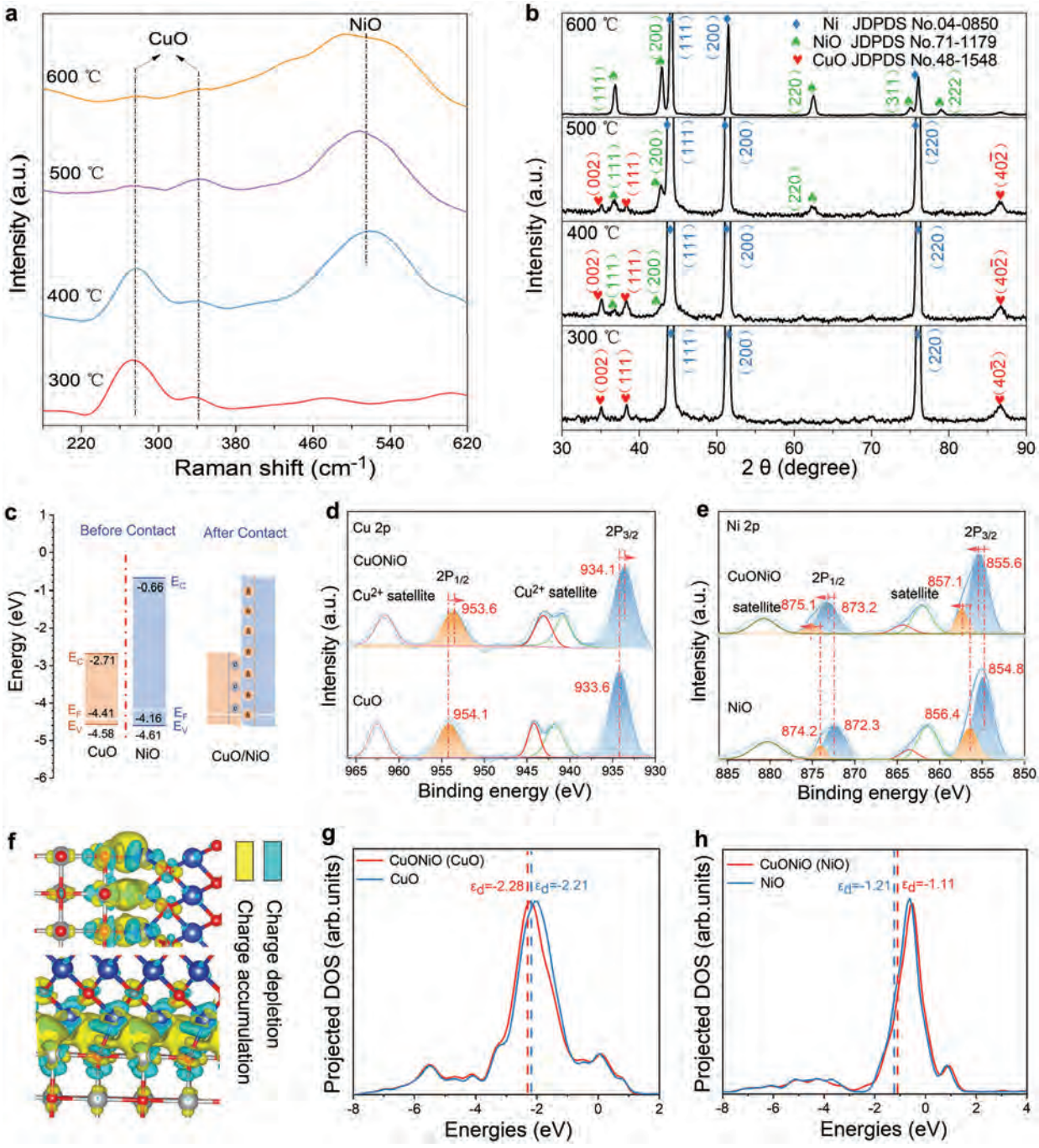

Figure 2. Chemical and electronic structures of CuO/NiO composites. a) Raman spectra and b) XRD pattern of CuO/NiO-300, CuO/NiO-400, CuO/NiO-500, and CuO/NiO-600. c) Energy band diagrams of CuO and NiO before contact and after formation of the CuO/NiO heterojunction. High-resolution XPS spectra of d) Cu 2p for CuO/NiO and CuO and e) Ni 2p for CuO/NiO and NiO. f) Calculated charge density difference of CuO/NiO. The Cu, Ni, and O atoms are marked in blue, grey, and red. The yellow and indigo blue regions represent the accumulation and depletion of charge density, respectively. g) Electronic density of states (DOS) calculated for CuO/NiO (CuO) and CuO. h) DOS calculated for CuO/NiO (NiO) and NiO.

d-band density of states (d-DOS).[39] Based on Figure 2g, we can see that the d-band center of CuO in the CuO/NiO heterostructure (−2.28 eV) shows a downshift compared with that in the pure-phased CuO (−2.21 eV). In contrast, the d-band center of the NiO-phase of the CuO/NiO heterostructure is about −1.11 eV, which is much closer to the Femi level compared to that of the pure-phased NiO (−1.21 eV) (Figure 2h). This altered DOS of the CuO-phase and NiO-phase of the CuO/NiO heterostructure may attribute to a various hybridization between the d orbitals of CuO/NiO and 2p orbitals of the absorbed NO_3^-RR intermediate species, thus exhibiting a considerable difference in the covalent interaction among them compared to that of CuO and NiO.[40,41]

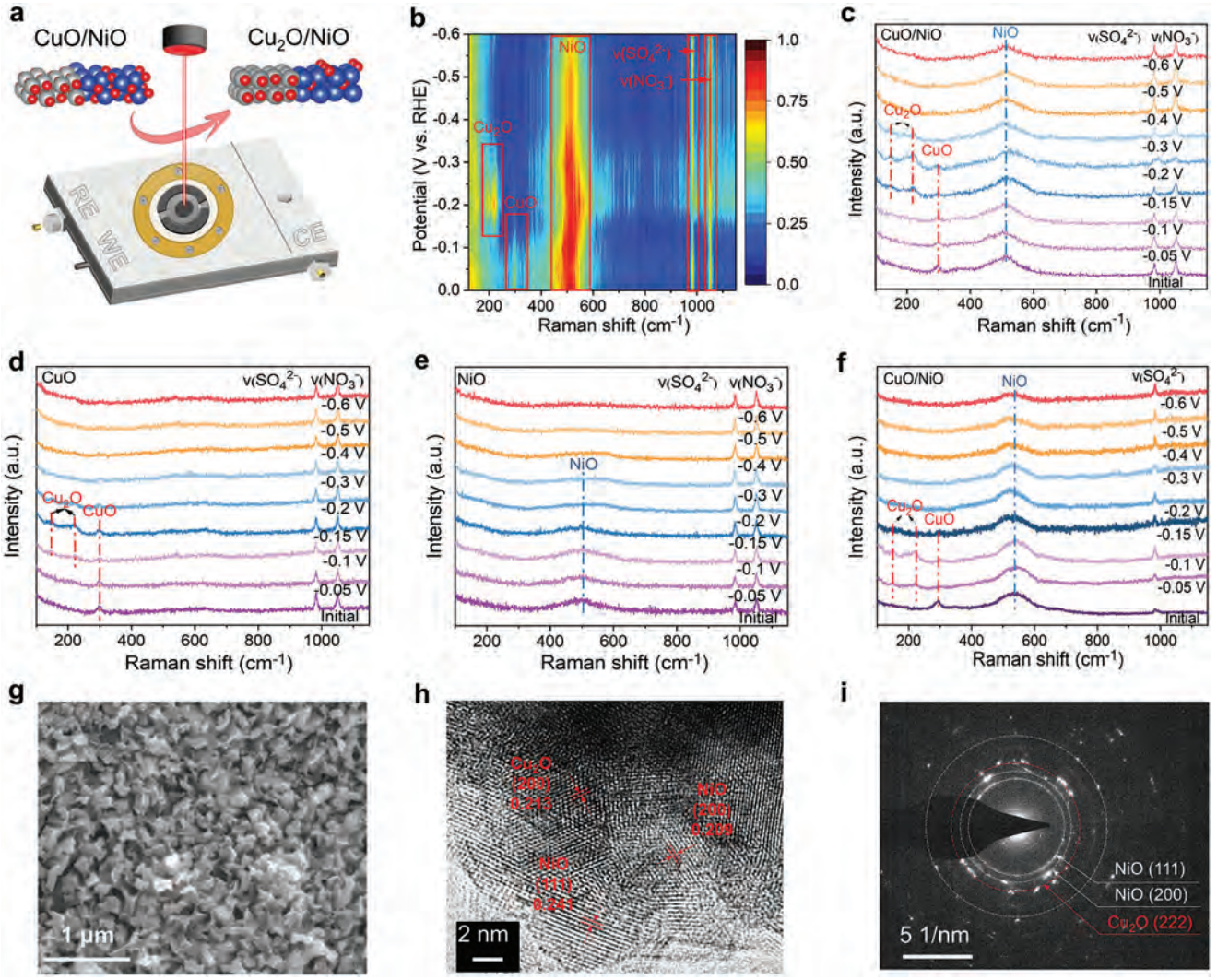

Figure 3. Identification of the reconstruction of CuO/NiO catalysts. a) Schematic illustration of in situ electrochemical Raman spectra of phase transformation of CuO/NiO during electrochemical NO_3^-RR process. In situ Raman spectra of the b,c) CuO/NiO catalyst, d) CuO, and e) NiO at different applied potentials in 0.5 M Na_2SO_4 electrolyte with 200 ppm NO_3^-–N. f) In situ Raman spectra of the CuO/NiO catalyst at different applied potentials in 0.5 M Na_2SO_4 electrolyte without NO_3^-–N. g) Surficial field-emission scanning electron microscope image of CuO/NiO catalysts after 2 h electrochemical reduction. h) HRTEM and i) SAED pattern of CuO/NiO catalysts after 2 h electrochemical reduction, where different component crystalline phases are marked out.

These characterizations and calculations, taken together, suggest that the interface of CuO/NiO heterostructures has the potential to improve the NO_3^-RR performance.

Electrocatalytic NO_3^--to-NH_3 conversion proceeds at reduction potentials, at which CuO/NiO catalysts suffer from potential-dependent phase reconstruction, leading to the formation of the multi-intermediate phase. In situ Raman spectroscopy was utilized to monitor the self-reconstruction behavior of the presynthesized CuO/NiO catalysts during this process (**Figure 3**a). $NaNO_3$ was added for the nitrate reduction test, and Na_2SO_4 was used as electrolyte. Raman spectroscopy of the CuO/NiO catalyst at different applied potentials (Figure 3b,c) show the initial characteristic peaks at 298 cm^{-1}, associated with CuO phases, persist at as low as −0.2 V versus RHE. Remarkably, at −0.15 V versus RHE, CuO phases gradually disappeared, and two sets of characteristic peaks of Cu_2O emerged at 148 and 218 cm^{-1}. Further decreasing the potential, the Raman signals of Cu_2O get weakened until they completely disappear, indicating a totally reduced Cu^0 phase.[18] Meanwhile, the broad Raman peaks of NiO appear at a wide range of around 510 cm^{-1} corresponding to the LO.[46] To further clarify the surface phase compositions during the whole NO_3^-RR, in situ Raman spectroscopy was applied to monitor the phase transformation under potentiostatic operation for 2 h at −0.2 V (Figure S6a, Supporting Information). The quickly attenuated CuO peak and the enhanced peak intensity of Cu_2O provide strong evidence of the partial reduction of CuO to Cu_2O during the first 10 min. With the prolonged reaction time, the peak of CuO disappears, while the Cu_2O peaks are maintained during the 2 h electrolysis, which impedes the initial CuO phase totally transferred to the stable Cu_2O phase as

the reaction progressed. The broad Raman peaks of NiO also remain unchanged. The coupling of Cu_2O and NiO could be confirmed as the main active catalyst for NO_3^--to-NH_3 conversion. For the phase transformation of the presynthesized CuO electrocatalyst, the Raman peak associated with Cu–O in the CuO catalyst quickly disappears, and the two sets of peaks assigned to the Cu_2O phase emerged at 148 and 218 cm^{-1} disappear at −0.15 V which is much higher than the active Cu_2O phase transformation potential in CuO/NiO (Figure 3d).[47] For the presynthesized NiO catalysts, the Ni–O mode in NiO is also rapidly attenuated with reducing potentials (Figure 3e). Additionally, the same but less notable Raman signals of Cu_2O and NiO were detected in the absence of NO_3^- (Figure 3f), partly owing to the NO_3^-RR delaying the electrochemical phase transformation.[18] The XPS further confirmed the stabilization of CuO/NiO surface phase compositions. Cu and Ni valence state variations along depth etching were further investigated (Figure S7, Supporting Information). Notably, as the etching depth increases, the peaks of Cu^{2+} and Ni^{3+} disappear from 0 to 20 nm, while those of Cu^+ and Ni^{2+} still persist in 100 nm, implying a small amount of Cu^{2+} and Ni^{3+} majorly located at the subsurface region. According to those results, we deduce that the emergence of Cu^{2+} and Ni^{3+} at the topmost sample surface can be attributed to the undesirable oxidation in ambient air. Thus, Cu_2O and NiO are the remaining phases after 2 h electrolysis.[48] Moreover, SEM images of CuO/NiO catalysts after 2 h electrochemical reduction suggest that the whole morphology is maintained, while the surface shows relatively sharp vertices and edges (Figure 3g). XRD patterns were as well collected to further reveal the transformation and stabilization of the Cu_2O/NiO heterostructure electrocatalyst (Figure S8, Supporting Information). The HRTEM image provides the lattice spacings of 0.213, 0.241, and 0.209 nm, which can be indexed to the (200) plane of Cu_2O and (111) and (200) planes of NiO (**Figure 4**h,i). To check out the possible changes of Cu^+, in situ Raman spectroscopy was utilized to monitor the self-reconstruction behavior of CuO/NiO catalysts during 10 cycles of electrolysis (2 h per cycle). Impressively, as shown in Figure S6 (Supporting Information), the peaks of Cu^+ shows no obvious change during the reaction of 10 cycles of NO_3^-RR, confirming its excellent stability. Thus, based on the above characterization results, in situ electrochemical self-reconstruction phenomenon of CuO/NiO heterostructure was confirmed, and Cu_2O/NiO could be the main active phase for NO_3^--to-NH_3 conversion.

In order to unveil the contributions of as-synthesized heterostructures towards the superior NO_3^-RR characteristics, an H-type electrolytic cell was constructed to measure and compare the performance of heterostructures in 200 ppm $NaNO_3$–N and 0.5 M Na_2SO_4 electrolyte (Figure 4a). Unless otherwise specified, all potentials were corrected versus the reversible hydrogen electrode. The original linear sweep voltammetry (LSV) curves were conducted to assess the intrinsic activity of the as-synthesized CuO/NiO, CuO, and NiO. The LSV curves in Na_2SO_4 electrolytes with and without $NaNO_3$ were investigated. The obviously enhanced current density for all the catalysts was attributed by the reduction of NO_3^- ions (Figure S9, Supporting Information). Interestingly, two distinct reduction peaks (peak R1 and R2) were observed in the curves of CuO/NiO and CuO. According to the previous study, the peak 1 (P_1) was allocated to the reduction of adsorbed NO_3^- ($*NO_3^-$) to adsorbed NO_2^- ($*NO_2^-$) corresponding to a two-electron transfer reaction (Equation 1), while the peak 2 (P_2) was assigned to the $*NO_2^-$ reduction into $*NH_3$ (Equation 2) corresponding to a six-electron transfer reaction.[49,50] After the second reduction peak (P_2), the current density seems to increase dramatically with the decrease of potential, which can be attributed to the hydrogen evolution reaction (HER).

$$* NO_3^- + H_2O + 2e^- \rightarrow * NO_2^- + 2OH^- \quad (1)$$

$$* NO_2^- + 5H_2O + 6e^- \rightarrow * NH_3 + 7OH^- \quad (2)$$

Further comparing the LSV curves of CuO/NiO, CuO, and NiO (Figure 4b), CuO/NiO, CuO appear to share a similar behavior toward NO_3^-RR at the initial stage of the reaction, indicating the important role of CuO in P_1 step. In the P_2 region, CuO/NiO displays a positive potential shift compared to CuO. Moreover, CuO/NiO yields the maximum current density of −33.5 mA cm^{-2} at a potential of −0.2 V versus RHE, which is 1.5 times of that of CuO and 7.1 times of that of NiO. CuO/NiO possesses a relatively larger current density than CuO and NiO, indicating the higher intrinsic activity of CuO/NiO. However, as the applied potential becomes negative, lower than −0.2 and −0.45 V, respectively, the current density of CuO/NiO and CuO decrease. The reason is that the surfaces are blocked by the adsorbed reduced intermediates and products until the surface is renewed.[18] However, the current density of CuO/NiO exhibits a slight and steady decrease compared to that of CuO, proving the combined NiO phases promptly eliminate the influence of toxic adsorbates. Moreover, the CuO/NiO exhibits a larger diffusion-limited maximum total current density (j_{total}) of −33.5 mA cm^{-2} than that of CuO. Thus, there is a synergy between the Ni-based and Cu-based phases in CuO/NiO for the highest NO_3^-RR activity, especially ranging from −0.15 to −0.4 V. This way, we chose −0.2 V as the operation voltage for further characterization of the NO_3^-RR products. A series of controlled-potential measurements were carried out to obtain FE of NH_3, assessing the partial current densities of NH_3 (Figure S10, Supporting Information). Benefiting from the great FE of NH_3 of CuO/NiO, it could reach a partial current density of NH_3 of 60.61 mA cm^{-2} at −0.6 V, much higher than that of CuO and NiO. To accurately derive the NO_3^--NH_3 conversion activities of catalysts, we normalize the partial current densities of NH_3 by the electrochemical active surface area (ECSA). We measured ECSA using the equation of ECSA = C_{dl}/C_{ref}, where C_{dl} is the double-layer capacity, and C_{ref} is assumed as 40 μF cm^{-2} as a moderate value for the specific capacitance of a flat surface.[51] The ECSA-normalized partial current densities of NH_3 are shown in Figure S11 (Supporting Information), which suggests the high intrinsic NO_3RR performance of CuO/NiO. With the prolonged electrolysis time, the concentration of NO_3^-–N kept decreasing from 200 ppm (−0.2 V, pH 7.20 at 0 min) to 21.1 ppm (−0.2 V, pH 13.50 at 120 min), whereas the concentration of NH_4^+–N continuously increasing to 158.3 ppm indicating a nitrate conversion efficiency of 89.5%, a NH_3 selectivity of 88.5% and a high NH_3 yield rate of 2.1 mol h^{-1} m^{-2} (Figure 4c; Figures S12–S15, Supporting Information). In particular, the concentration of NO_2^- products remains low during the electrolysis, which further confirms the high selectivity to NH_3. As depicted in Figure S16 (Supporting Information), the catalytic current obviously decreased

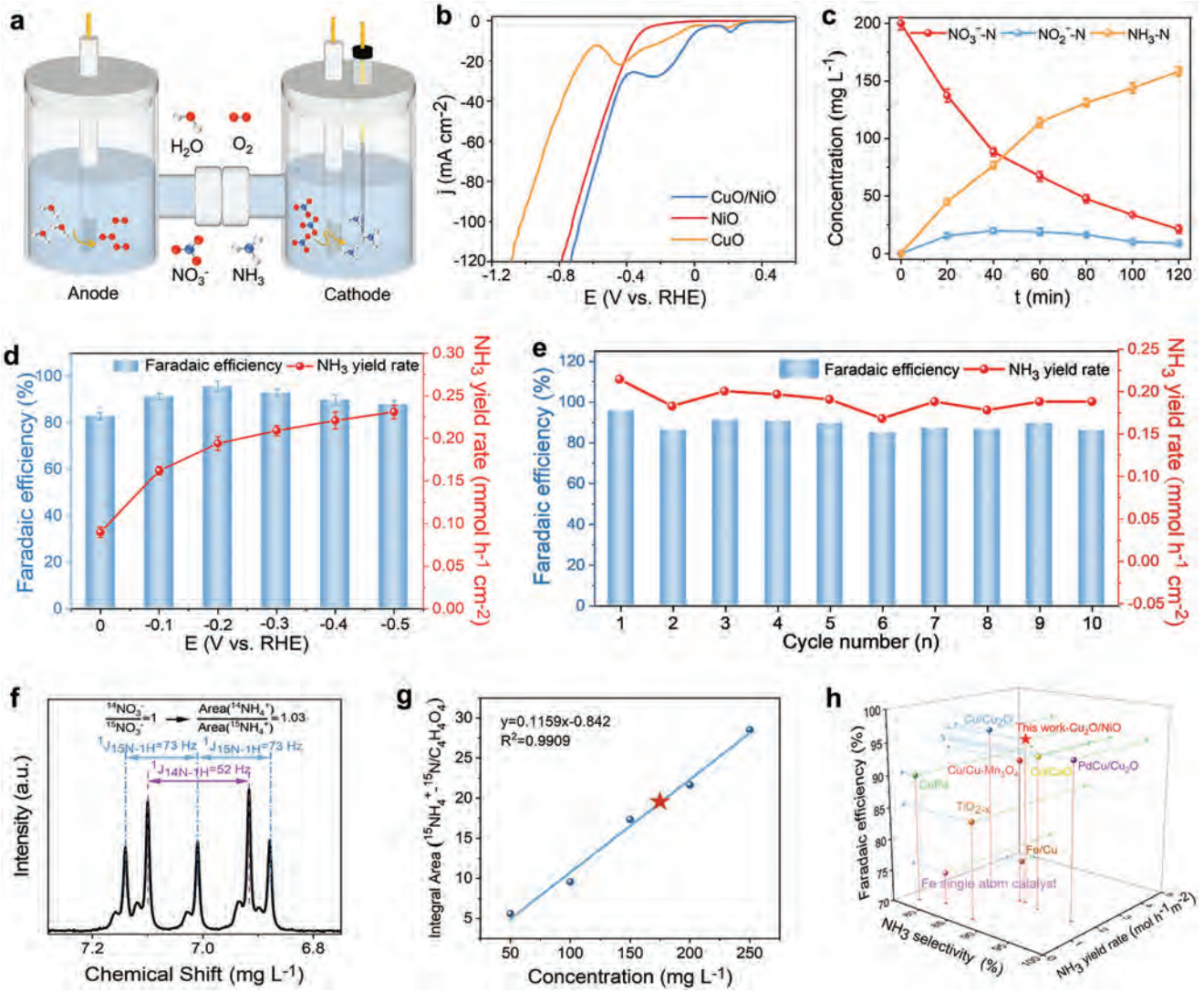

Figure 4. Electrocatalytic NO_3^--to-NH_3 conversion over CuO/NiO. a) Schematic illustration of electrochemical NO_3^-RR in an H-type electrolytic cell. b) LSV curves of CuO/NiO, CuO, and NiO in 0.5 M Na_2SO_4 electrolyte with 200 ppm NO_3^-–N upon a scan rate of 5 mV s^{-1}. c) Time-dependent concentration change of NO_3^-, NO_2^-, and NH_3 over CuO/NiO. d) The FE and yield rate of NH_3 at different applied potentials in 0.5 M Na_2SO_4 electrolyte with 200 ppm NO_3^-–N over a CuO/NiO cathode. e) The FE and yield rate of NH_3 in consecutive recycling tests over a CuO/NiO cathode. f) The ^1H NMR spectra of the electrolyte after NO_3^-RR by using $^{14}NO_3^-$–^{14}N / $^{15}NO_3^-$–^{15}N as the nitrogen source. g) The standard curve of the integral area against $^{15}NH_4^+$–^{15}N concentration. h) Comparison of NH_3 Faradaic efficiency, NO_3^- to NH_3 selectivity and NH_3 yield rate for recently reported state-of-the-art NO_3RR electrocatalysts including Cu/Cu_2O,[16] $PdCu/Cu_2O$,[42,43] $Cu/Cu–Mn_3O_4$,[28] Co/CoO,[44] CuPd,[29] TiO_{2-x},[45] Fe/Cu,[46] and Fe single atom catalyst.[27]

during the first 1 h of electrolysis and then showed slight degradation with the prolonged reaction time. The special chronoamperometric curve (*i*–*t*) should be attributed to the slowdown of the reaction rate. In the NO_3^-RR process, the concentration of NO_3^- keeps decreasing with the accumulated NH_3 in the electrolyte (Figure 4c), which impedes this catalytic reaction by constraining the kinetic mass transfer of NO_3^-, resulting in the worse catalytic activity with the prolonging of electrolysis time. As depicted in Table S1 (Supporting Information), the NO_3^-–N removal rate slows down with the increased electrolysis time. The higher removal rate in the first hour means the quick reduction of nitrate. In that way, the catalytic current exhibits a sharp degradation because the current is related to the nitrate concentration. From 0 to −0.5 V versus RHE, the yield rate of NH_3 gradually increases while the Faradaic efficiency curve shows a volcanic shape with a maximum value of 95.6% at −0.2 V (Figure 4d). Here, the slight deterioration of Faradaic efficiency at more negative potentials is caused by the competing HER. The Faradaic efficiency and ammonia yield show no obvious descending tendency after ten cycles of 2 h electrocatalytic NO_3^-RR reaction, confirming its excellent stability (Figure 4e). To trace the source of NH_3, isotope labeling experiments were conducted by adding $^{15}NO_3^-$ as the N source. ^1H nuclear magnetic resonance (NMR) spectroscopy exhibited doublet patterns, and the coupling constant of 73 Hz corresponded to the signal of $^{15}NH_4^+$. There is no signal of $^{14}NH_4^+$ confirming strong evidence that the obtained NH_3

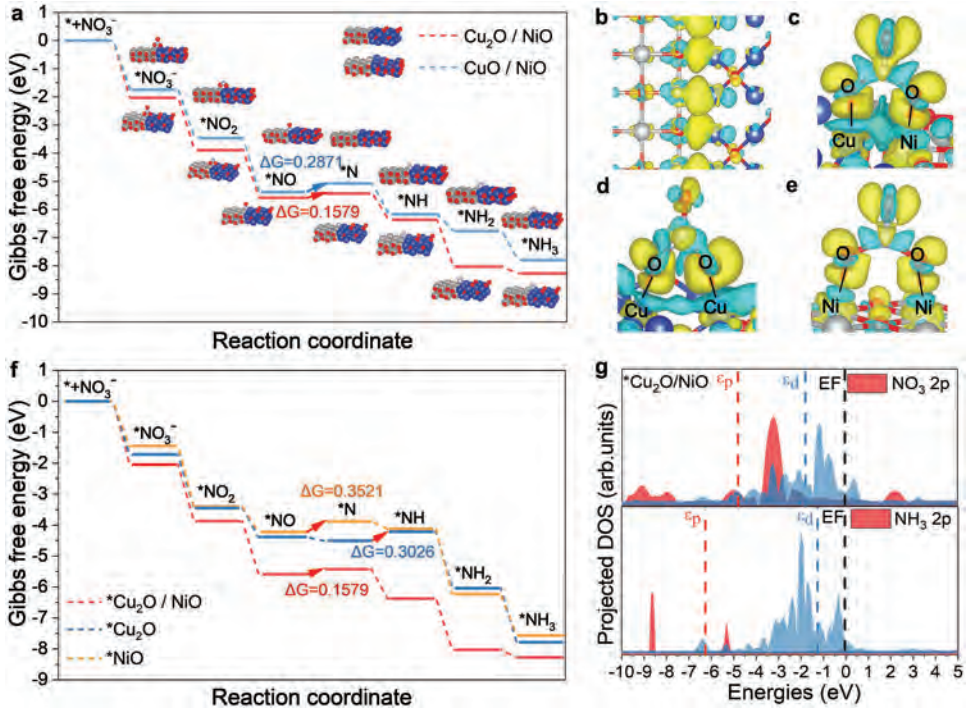

Figure 5. DFT calculations for the electronic structures and reaction mechanism. a) Free-energy diagrams for NO_3^-RR on the interface of Cu_2O/NiO (red line) and the interface of CuO/NiO (blue line) at U=0 V. b) Calculated charge density difference of Cu_2O/NiO. The Cu, Ni, and O atoms are marked in blue, grey, and red. c–e) Charge density difference for NO_3^* adsorption on Cu_2O/NiO, Cu_2O, and NiO. f) Free-energy diagrams for NO_3^-RR on the interface of Cu_2O/NiO (red line), Cu_2O region in Cu_2O/NiO (blue line), and NiO region in Cu_2O/NiO (yellow line) at U = 0 V. g) PDOS calculated for NO_3^* and NH_3^* adsorption on Cu_2O/NiO.

originated from the electrolysis of $^{15}NO_3^-$ instead of any other ammonia pollution (Figure S17a, Supporting Information). Furthermore, adding $^{14}NO_3^-/^{15}NO_3^-$ in a ratio of 1 to 1, the unchanged ratio of $^{14}NH_4^+/^{15}NH_4^+$ after the electrocatalytic reduction once again identifies added NO_3^- is the only source of nitrogen during the reduction process here (Figure 4f). The concentration of NH_3 calculated by the ^{1}H NMR and colorimetric methods are nearly equal, evidently proving the accuracy of the two quantitative methods (Figure 4g; Figure S17b, Supporting Information). The achieved NO_3^-RR activity over CuO/NiO is also superior to most reported catalysts (Figure 4h).

To further understand the catalytic activity of NO_3^-RR on CuO/NiO and Cu_2O/NiO, the rate-determining step (RDS) energy barriers on those two catalysts are calculated in **Figure 5**a. The results indicate that the RDS energy barrier of nitrate conversion on CuO/NiO is higher than that on Cu_2O/NiO, proving a more favorable nitrate reduction reaction on Cu_2O/NiO. Therefore, the above calculation evidence that Cu_2O/NiO is the active phase for NO_3^-RR. DFT calculations were performed to reveal the electronic structures of Cu_2O/NiO heterostructures and the origin of the enhanced NO_3^-RR performance. The interface model bridging the Cu_2O (200) and NiO (200) surfaces was built according to the observed crystalline lattice planes in HRTEM images of the catalysts after electrolysis (Figure 3h). As the charge density difference for Cu_2O/NiO depicted in Figure 5b, abundant charge (the yellow area) accumulated at the interface between Cu_2O and NiO indicates that most of the charge transfer in Cu_2O/NiO occurs at the interface.[52] That is, electron-coupled interactions between Cu_2O and NiO phases similar to the above CuO/NiO heterostructure can change the electron distribution at the interface and optimize the electronic structure of Cu_2O/NiO, thus enhancing the NO_3^-RR catalytic activity. Additionally, the charge density difference between before and after adsorption of NO_3^- on the interface of Cu_2O/NiO (*Cu_2O/NiO), on the surface of Cu_2O phase (*Cu_2O) and NiO phase (*NiO) of Cu_2O/NiO were evaluated (Figure 5c–e), respectively.[53] The calculation results exhibited more obvious charge transfer from the oxygen atoms of NO_3^- to Cu sites and Ni sites at the interface of Cu_2O/NiO, providing powerful clues to a stronger interaction between *NO_3 and the interface region of Cu_2O/NiO. Furthermore, Gibbs free energy of NO_3^-RR process was calculated by a series of deoxidation steps (*NO_3^- → *NO_2 → *NO → *N) and several hydrogenation steps (*N → *NH → *NH_2 → *NH_3) based on previous study.[54] As depicted in Figure 5f and Figure S18 (Supporting Information), the RDS of NO_3^-RR for *Cu_2O/NiO and *NiO was the reduction of NO* to N* with the differences of Gibbs free energies (ΔG) of 0.16 and 0.35 eV, respectively. However, the RDS of NO_3^-RR should be hydrogenation of *N to *NH for *Cu_2O with ΔG of 0.30 eV (Figure 5e), thus the RDS of NO_3^-RR for *Cu_2O/NiO is much easier to occur. Similar to the results of charge density difference diagrams, ΔG of the adsorption of *NO_3 on the interface of Cu_2O/NiO ($\Delta G = -2.04$ eV) is higher than the one of *NiO ($\Delta G = -1.45$ eV) and *Cu_2O ($\Delta G = -1.72$ eV), which displays that the interface of Cu_2O/NiO is the optimal active sites for the absorption of NO_3^-. The LSR in the multistep reactions means the binding of reactants and

products are scaled linearly;[55] in other words, strong adsorption of reaction intermediates will likely lead to the strong adsorption of products, therefore impeding the reaction considerably.[56] The LSR says that in an 8-electron transfer NO_3^-RR reaction, the adsorption energies of reactants NO_3^- and products NH_3 are linearly linked.[35,57] That is, strong adsorption of NO_3^- resulted in strong NH_3 adsorption, thus decelerating NH_3 release and lead to surface poisoning. Whereas too weak adsorption results in a large energy barrier of NO_3^- adsorption and thus slows down the reaction. Thus, the PDOS (Figure 5g) profiles for NO_3^- adsorption and NH_3 desorption were studied. The energy difference (ΔE) between 3d band center (ϵ_d) of the Cu site and Ni site at the interface of Cu_2O/NiO (*Cu_2O/NiO) and NO_3^- 2p band center (ϵ_p) was calculated to be 2.93 eV. As a comparison, ΔE (4.27 eV) between ϵ_d of *Cu_2O/NiO and ϵ_p of NH_3 is much larger than that of absorbed NO_3^-.[42] This finding indicates that Cu_2O/NiO possesses a strong *Cu_2O/NiO 3d-NO_3^- 2p orbital hybridization and a weak orbital hybridization between *Cu_2O/NiO 3d and NH_3 2p. Based on previous studies, the strong orbital hybridization between *Cu_2O/NiO and NO_3^- indicates a higher Cu–O and Ni–O covalency, and the weak orbital hybridization means NH_3 product can easily release from the active sites. Thus, the appropriate orbital hybridization with NO_3^- and NH_3 endow Cu_2O/NiO with superior NO_3^-RR performance. To further understand the synergistic role of Cu_2O and NiO for NO_3^-RR, the orbital hybridization of NO_3^- and NH_3 with Cu_2O and NiO were compared (Figure S19, Supporting Information). The calculated results show that the lower ΔE between ϵ_d of Cu_2O and ϵ_p of NO_3^- and the larger ΔE for NiO 3d-NH_3 2p orbital hybridization, suggesting Cu_2O considerably enhances NO_3^- adsorption, while NiO could promote the desorption of NH_3. This calculation results match well with the LSV experiment results (Figure 4b). Therefore, taking together the computational and experimental results, the reconstructed active phase Cu_2O/NiO modulates the local electronic structures and possesses the tandem effect of Cu_2O and NiO, thus leading to the efficient nitrate to ammonia electrosynthesis at low overpotentials.

3. Conclusion

In summary, we have synthesized the stabilized intermediate phase of transition metals oxide heterostructures via electrochemical redox activation-induced phase reconstruction strategy for efficient ammonia electrosynthesis. The experimental and theoretical calculations reveal that the intermediate coupling phases induce electron redistribution and dramatically lower the overpotential in the rate-determining step. Moreover, the calculations of orbital hybridization reveal that NO_3^- adsorption is considerably enhanced by Cu_2O, while NiO could promote the desorption of NH_3 and thus promptly renew the surface. Those two cooperative catalytic sites enable high efficiency and selectivity for NH_3 electrosynthesis. When the applied potential is −0.2 V, the reconstructed and stabilized Cu_2O/NiO catalysts exhibit an excellent NH_3 FE of 95.6%, a super-high NH_3 selectivity of 88.5%, and the ammonia-evolving rate of 2.1 mol h^{-1} m^{-2}, outperforming most of the reported catalysts at the same electrocatalytic conditions. Importantly, this study provides a systematic strategy to analyze and stabilize the active intermediate phase of CuO/NiO catalysts for efficient ammonia electrosynthesis, contributing to an in-depth understanding of the accurate electrocatalytic mechanisms.

4. Experimental Section

Preparation of the CuO/NiO@NF Electrode: The CuO/NiO@NF electrode was prepared through two steps: (i) The Cu–NF electrode was synthesized through galvanic replacement between Ni and $CuSO_4$ on a NF matrix driven by the difference in the reduction potentials of Cu versus Ni. (ii) The Cu-doped NF electrode was converted into CuO/NiO@NF via an annealing treatment. Before galvanic replacement, the nickel foam (3.0 × 1.0 cm) was sonicated in HCl solution (1 M) for 10 min to remove the NiO surface layer and followed by rinsing with water and acetone for three times, then allowed to blow-dry in with the nitrogen gas. The galvanic replacement was carried out by dipping the cleaned NF into 50×10^{-3} M $CuSO_4$ solutions and kept for 30 min. The obtained Cu–NF electrode was finally annealed at 300, 400, 500, and 600 °C for 30 min in an air atmosphere, where they were abbreviated as CuO/NiO-300, CuO/NiO-400, CuO/NiO-500, and CuO/NiO-600, respectively. The CuO@NF and NiO@NF electrodes were prepared through directly annealing copper foam (CF) and NF for 30 min at 400 °C under the air atmosphere.

Characterization: SEM images and EDX spectra were obtained with FEI Quanta 450 FESEM analysis system. The cross-sectional sample was artificially precut and prepared vertically with a sharp scissor. Moreover, high-resolution transmission electron microscopy (HRTEM), selected area electron diffraction (SAED), and elements mapping were obtained with JEOL JEM-2100F equipment. Raman spectroscopy was employed in a WITec alpha 300 R Raman System with a 532 nm laser excitation source. The crystalline structure was confirmed by Powder X-ray diffraction with a Bruker D8 Focus Diffraction System with a monochromatized Cu-Kα radiation source ($\lambda = 0.1541$ nm). The elemental composition and valance state were measured on X-ray photoelectron spectroscopy (XPS) analyses equipped with a PHI 5000 Versaprobe system and monochromatic Al Kα radiation. All binding energies were calibrated on the C 1s peak at 284.8 eV. Ultraviolet photoelectron spectroscopy (UPS) measurements were performed with an He I (21.22 eV) line as an excitation source. The work function was examined by the secondary electron cut-off (E_{cutoff}) in the UPS spectrum (equivalent to 21.22 eV-E_{cutoff}). The valence band maximum was determined from the low binding energy onset. The conduction band edge energy positions of CuO and NiO were determined by E_V and the energy gap (E_g) obtained in the reported literature.[33] Isotope labeling experiments were carried out on nuclear magnetic resonance measurement (Bruker 400-MHz system).

Electrochemical Measurements: All the electrochemical measurements were conducted on a CHI660D electrochemical workstation in an H-type electrolytic cell separated by a Nafion 117 membrane. The CuO/NiO@NF (1×1 cm), platinum foil, and saturated Ag/AgCl electrode acted as the working electrode, counter electrode, and reference electrode, respectively. 0.5 M Na_2SO_4 solution (40 mL) was used as catholyte and anolyte. 200 ppm nitrate-N was also added into the cathode compartment for the nitrate reduction test. All the solutions used in the electrochemical nitrate reduction were purged with high-purity nitrogen for 10 min. Before the nitrate electroreduction test, linear sweep voltammetry curves were recorded at a rate of 5 mV s^{-1}. For nitrate electroreduction experiments, potential-controlled measurements were conducted for 2 h in each potential at a stirring rate of 400 rpm. Three replicate electrochemical experiments were conducted on each sample to determine the error bar. The electrolyte was collected to identify the product of nitrate reduction by the UV–vis spectrophotometer.[58]

The potential (versus saturated Ag/AgCl) was converted to RHE using the Nernst Equation (3):

$$E_{RHE} = E_{Ag/AgCl} + 0.0591 \times pH + E^0_{Ag/AgCl} \left(E^0_{Ag/AgCl.} = 0.197\right) \quad (3)$$

Determination of NO_3^-: An amount of electrolyte was collected and diluted to the range of detection. Then, the diluted electrolyte (10 mL) was mixed well with 100 µL 1 M HCl and 10 µL 0.8 wt% sulfamic acid solution.

The absorption spectrum of NO_3^- was determined at 220 and 275 nm by an UV–vis spectrophotometer. The absorbance value at 220 nm detected both organic nitrate and chemical signals, while the absorbance value at 275 nm only contained signals from the organics. The final absorbance value was calculated by the absorbance at 220 nm minus the absorbance at 275 nm. In order to quantify the concentration, the concentration-absorbance curve was plotted using a series of standard KNO_3 solutions.

Determination of NO_2^-: The concentration of NO_2^- was determined by Griess method. The color reagent of Griess method was prepared as follows: adding 4 g *p*-aminobenzene sulfonamide and 0.2 g *N*-(1-naphthyl) ethylenediamine dihydrochloride to the mixed solution of 10 mL phosphoric acid and 50 mL deionized water. A certain amount of electrolyte was diluted to the detection range and 5 mL diluted electrolyte was added with 100 µL color reagent. After standing for 20 min in a dark place, the absorbance value at a wavelength of 540 nm was determined by UV–vis absorption spectra. The concentration–absorbance curve was calibrated using a series of standard concentration KNO_2 solutions.

Determination of NH_3: Similar to the method of confirming the concentration of NO_3^- and NO_2^-, NH_3 was determined by the indophenol blue approach. First, a certain amount of electrolyte was diluted to the detection range. Then, 3 mL diluted electrolyte was taken out into a test tube. Next, 1 mL 2.0 M NaOH solution containing 10.0 wt% sodium citrates ($C_6H_5Na_3O_7{\cdot}2H_2O$) and 10.0 wt% salicylic acid ($C_7H_6O_3$) was added and mixed thoroughly, followed by adding 1 mL 0.05 M NaClO solution and 0.2 mL 1.0 wt% sodium nitroferricyanide ($Na_2[Fe(NO)(CN)_5]{\cdot}2H_2O$) solution. The absorbance value at a wavelength of 658 nm was recorded after sitting for 2 h. The concentration-absorbance calibration curve was calibrated using a series of standard concentration $NH_4(SO_4)_2$ solutions.

Calculation of the Faradaic Efficiency and Yield Rate: Faradaic efficiency of NH_3 was calculated by using Equation (4):

$$FE_{NH_3}(\%) = \frac{8F \times c_{NH_3} \times V}{17 \times Q} \tag{4}$$

NH_3 yield rate was calculated by using Equation (5):

$$NH_3 \text{yieldrate}\left(\text{mgh}^{-1}\text{cm}^{-2}\right) = \frac{c_{NH_3} \times V}{t \times s} \tag{5}$$

The percentage of NO_3^- conversion was calculated by using Equation (6):

$$NO_3^- \text{conversion}(\%) = \frac{c_o \times c_t}{c_o} \times 100 \tag{6}$$

The NH_3 selectivity was evaluated by using Equation (7):

$$NH_3 \text{selectivity} = \frac{X_i}{c_o \times c_t} \times 100 \tag{7}$$

where F is Faraday constant (96485 C mol^{-1}), c_{NH3} (mg L^{-1}) is the NH_3 concentrations after electrolysis at the reduction time t, V (mL) is the volume of the cathodic electrolyte, Q (C) is the overall charge passing the electrode, s is the geometric area of catalyst (cm^2), c_0 and c_t are the measured NO_3^- concentrations before and after electrolysis at the reduction time t, and X_i is the concentration of NH_3 after electrolysis.

In Situ Raman Spectroscopy: In situ Raman spectroscopy was performed by the aforementioned Raman microscope and a three-electrode electrochemical cell. A Pt wire and Ag/AgCl electrode were used as counter and reference electrodes, respectively. CuO/NiO and CuO electrodes were used as working electrodes and immersed into the 0.5 M Na_2SO_4 electrolyte to ensure sufficient ionic conductivity. The existence and nonexistence of 200 ppm nitrate-N were also tested as a contrast.

^{14}N Isotope-Labeling Experiment: The isotope-labeling nitrate reduction experiments were conducted on a Bruker 400 MHz Nuclear Magnetic Resonance System. 98.5% $Na^{15}NO_3$ was used as the feeding N-source and 0.5 M Na_2SO_4 was used as the electrolyte. After electroreduction, the obtained electrolyte (25 mL) containing $^{15}NH_4^+ - ^{15}N$ was taken out and adjusted to be weak acid with H_2SO_4, followed by mixing with 0.01 g maleic acid ($C_4H_4O_4$) as an internal standard. Then, 50 µL deuterium oxide (D_2O) was added to 0.5 mL above solution for the NMR detection. 50, 100, 150, 200, and 250 ppm $^{15}NH_4^+ - ^{15}N$ were prepared for achieving the calibration curve. Similarly, $Na^{14}NO_3/Na^{15}NO_3$ equals to 1:1 was also used as N-source in the nitrate reduction methods, and then the ratio of products $^{14}NH_4^+ - ^{14}N$/ $^{15}NH_4^+ - ^{15}N$ was quantified by NMR detection to further clarify the source of ammonia.

Computational Details: The first principles density functional theory (DFT) calculations were carried out using the Vienna ab initio Simulation Package (VASP) and the Perdew–Burke–Ernzerhof (PBE) functional within generalized gradient approximation (GGA).[59] The projector-augmented wave (PAW) method was applied in plane waves with a cutoff energy of 500 eV. The 3×3×1 k-point mesh set was used for geometry optimization, self-consistent, and the density of states (DOS) calculations. A vacuum layer of 15 Å was used for Cu_2O/NiO (200), Cu (100), and Ni (100) slab models. The crystal Cu_2O/NiO was constructed by cleavage of (200) surface according to the TEM results. Cu (100) and Ni (100) are the most active surface for the electrochemical NO_3^- reduction.[60] In all calculations, the electronic iterations convergence was optimized to 10^{-5} eV with the Hellmann–Feynman forces of 0.02 eV $Å^{-1}$. VESTA and VASPKIT were applied to obtain the DOS diagrams.[61]

The NO_3^- reduction process can be described as following Equations (8)–(15):

$$* + NO_3^- \rightarrow * NO_3 + e^- \tag{8}$$

$$* NO_3 + H_2O + e^- \rightarrow * NO_2 + 2OH^- \tag{9}$$

$$* NO_2 + H_2O + 2e^- \rightarrow * NO + 2OH^- \tag{10}$$

$$* NO + H_2O + 2e^- \rightarrow * N + 2OH^- \tag{11}$$

$$* N + H_2O + e^- \rightarrow * NH + OH^- \tag{12}$$

$$* NH + H_2O + e^- \rightarrow * NH_2 + OH^- \tag{13}$$

$$* NH_2 + H_2O + e^- \rightarrow * NH_3 + OH^- \tag{14}$$

$$* NH_3 \rightarrow NH_3 + * \tag{15}$$

where * represents the active site. The reaction free energy change was calculated as follows (Equation (16)):

$$\Delta G = \Delta E + \Delta E_{ZPE} - -T\Delta S \tag{16}$$

where ΔE is the total energy difference. ΔE_{ZPE} and ΔS are the corrections of the zero-point energy and entropy, which are obtained from the vibrational frequency calculations. T is the temperature and equals to 298.15 K.

To avoid calculating the energy of charged NO_3^- directly, HNO_3(g) is chosen to be a reference as below Equations (17) and (18):

$$HNO_3\ (g) \rightarrow HNO_3\ (l) \tag{17}$$

$$HNO_3\ (l) \rightarrow H^+ + NO_3^- \tag{18}$$

Hence, the Equation (6) can be rewritten as below (Equation (19)):

$$* + HNO_3 \rightarrow * NO_3 + H^+ + e^- \tag{19}$$

The Gibbs free energy of NO_3 ($\Delta G(*NO_3)$) is described as (Equation (20)):

$$\Delta G\,(NO_3\ *) = G\,(*\ NO_3) - G\,(HNO_3) + \frac{1}{2}G\,(H_2) - G\,(*) + \Delta G_{correct} \tag{20}$$

in which $G(*NO_3)$, $G(HNO_3)$, and G (*) are the DFT-calculated Gibbs free energy of adsorbed nitrate, HNO_3, and catalysts, respectively. $\Delta G_{correct}$ is the correction of adsorption energy.

Supporting Information

Supporting Information is available from the Wiley Online Library or from the author.

Acknowledgements

This work was financially supported by the City University of Hong Kong (project no. 9667227, 9678244 and 9231502).

Conflict of Interest

The authors declare no conflict of interest.

Author Contributions

D.Y. conceived the idea and led the project. W.W., W.J.W., and Y.M. processed the sample growth and structural characterization. D.C. and Q.Q. processed the electrochemical measurements. D.Y. and Y.X. Zhang conducted DFT calculations. X.Y.W, X.M.B., and J.C.H validated the experimental results and performed data curation. D.Y. wrote the manuscript. All authors made revisions and approved the manuscript.

Data Availability Statement

The data that support the findings of this study are available from the corresponding author upon reasonable request.

Keywords

electrochemical nitrate reduction, heterostructures, phase transformation, tandem effects

Received: April 5, 2023
Revised: July 7, 2023
Published online: August 17, 2023

[1] A. Martín, T. Shinagawa, J. Pérez-Ramírez, *Chem* **2018**, *5*, 2602.
[2] P. Langevelde, I. Katsounaros, M. Koper, *Joule* **2021**, *5*, 290.
[3] J. G. Chen, R. M. Crooks, L. C. Seefeldt, K. L. Bren, R. M. Bullock, M. Y. Darensbourg, P. L. Holland, B. Hoffman, M. J. Janik, A. K. Jones, *Science* **2018**, *360*, 6611.
[4] G. Zhigang, L. Yan, K. Xiangdong, L. i. Pai, Z. Kan, *Adv. Mater.* **2018**, *40*, 1803498.
[5] B. H. R. Suryanto, H. L. Du, D. B. Wang, J. Chen, A. N. Simonov, D. R. MacFarlane, *Nat. Catal.* **2019**, *2*, 290.
[6] C. D. Lv, C. S. Yan, G. Chen, Y. Ding, J. X. Sun, Y. S. Zhou, G. H. Yu, *Angew. Chem., Int. Ed.* **2018**, *57*, 6073.
[7] J. Li, G. M. Zhan, J. H. Yang, F. J. Quan, C. L. Mao, Y. Liu, B. Wang, F. C. Lei, L. J. Li, A. W. M. Chan, L. P. Xu, Y. B. Shi, Y. Du, W. C. Hao, P. K. Wong, J. F. Wang, S. X. Dou, L. Z. Zhang, J. C. Yu, *J. Am. Chem. Soc.* **2020**, *142*, 7036.
[8] Y. T. Wang, Y. F. Yu, R. R. Jia, C. Zhang, B. Zhang, *Natl. Sci. Rev.* **2019**, *6*, 730.
[9] Z. Y. Wu, M. Karamad, X. Yong, Q. Z. Huang, D. A. Cullen, P. Zhu, C. A. Xia, Q. F. Xiao, M. Shakouri, F. Y. Chen, J. Y. Kim, Y. Xia, K. Heck, Y. F. Hu, M. S. Wong, Q. L. Li, I. Gates, S. Siahrostami, H. T. Wang, *Nat. Commun.* **2021**, *12*, 2870.
[10] S. H. Ye, Z. D. Chen, G. K. Zhang, W. D. Chen, C. Peng, X. Y. Yang, L. R. Zheng, Y. L. Li, X. Z. Ren, H. Q. Cao, D. F. Xue, J. S. Qiu, Q. L. Zhang, J. H. Liu, *Energy Environ. Sci.* **2022**, *15*, 760.
[11] D. Yin, Y. Y. Liu, P. F. Song, P. Chen, X. Liu, L. K. Cai, L. H. Zhang, *Electrochim. Acta* **2019**, *324*, 134846324.
[12] H. M. Liu, X. Y. Lang, C. Zhu, J. Timoshenko, M. Ruscher, L. C. Bai, N. Guijarro, H. B. Yin, Y. Peng, J. H. Li, Z. Liu, W. C. Wang, B. Roldan Cuenya, J. S. Luo, *Angew. Chem., Int. Ed.* **2022**, *61*, 256.
[13] D. Reyter, D. Belanger, L. Roue, *Electrochim. Acta* **2008**, *53*, 5977.
[14] F. Y. Chen, Z. Y. Wu, S. Gupta, D. J. Rivera, S. V. Lambeets, S. Pecaut, J. Y. T. Kim, P. Zhu, Y. Z. Finfrock, D. M. Meira, G. King, G. H. Gao, W. Q. Xu, D. A. Cullen, H. Zhou, Y. M. Han, D. E. Perea, C. L. Muhich, H. T. Wang, *Nat. Nanotechnol.* **2022**, *17*, 759.
[15] J. X. Liu, D. Richards, N. Singh, B. R. Goldsmith, *ACS Catal.* **2019**, *9*, 10846.
[16] Y. T. Wang, W. Zhou, R. R. Jia, Y. F. Yu, B. Zhang, *Angew. Chem., Int. Ed.* **2020**, *59*, 5350.
[17] Y. H. Wang, A. Xu, Z. Y. Wang, L. S. Huang, J. Li, F. W. Li, J. Wicks, M. C. Luo, D. H. Nam, C. S. Tan, Y. Ding, J. W. Wu, Y. W. Lum, C. T. Dinh, D. Sinton, G. F. Zheng, E. H. Sargent, *J. Am. Chem. Soc.* **2020**, *142*, 5702.
[18] M. Xu, Q. Xie, D. Duan, Y. Zhang, Y. Zhou, H. Zhou, X. Li, Y. Wang, P. Gao, W. Ye, *ChemSusChem* **2022**, *11*, 202200231.
[19] R. D. Milton, S. D. Minteer, *ChemPlusChem* **2017**, *82*, 513.
[20] H. Wang, Q. Mao, T. Ren, T. Zhou, K. Deng, Z. Wang, X. Li, Y. Xu, L. Wang, *ACS Appl. Mater. Interfaces* **2021**, *13*, 44733.
[21] N. Comisso, S. Cattarin, S. Fiameni, R. Gerbasi, L. Mattarozzi, M. Musiani, L. Vazquez-Gomez, E. Verlato, *Electrochem. Commun.* **2012**, *25*, 91.
[22] L. Mattarozzi, S. Cattarin, N. Comisso, P. Guerriero, M. Musiani, L. Vazquez-Gomez, E. Verlato, *Electrochim. Acta* **2013**, *89*, 488.
[23] X. Yao, B. Yu, Y. Xue, X. Ran, J. Zuo, K. Qiu, *J. Water Process Eng.* **2021**, *42*, 102174.
[24] S. Jung, S. Bae, W. Lee, *Environ. Sci. Technol.* **2014**, *48*, 9651.
[25] H. Xu, J. Wu, W. Luo, Q. Li, W. X. Zhang, J. P. Yang, *Small* **2020**, *16*, 2001775.
[26] Q. Hu, Y. Qin, X. Wang, Z. Wang, X. Huang, H. Zheng, K. Gao, H. Yang, P. Zhang, M. Shao, *Energy Environ. Sci.* **2021**, *14*, 4989.
[27] Z. Y. Wu, M. Karamad, X. Yong, Q. Huang, D. A. Cullen, P. Zhu, C. Xia, Q. Xiao, M. Shakouri, F. Y. Chen, *Nat. Commun.* **2021**, *12*, 2870.
[28] H. Ding, H. Liu, W. Chu, C. Wu, Y. Xie, *Chem. Rev.* **2021**, *121*, 13174.
[29] Y. Xu, K. Ren, T. Ren, M. Wang, M. Liu, Z. Wang, X. Li, L. Wang, H. Wang, *Chem. Commun.* **2021**, *57*, 7525.
[30] P. Ling, Y. Liu, Z. Wang, L. Li, J. Hu, J. Zhu, W. Yan, H. Jiang, Z. Hou, Y. Sun, *Nano Lett.* **2022**, *22*, 2988.
[31] C. Hu, Y. Hu, C. Fan, L. Yang, Y. Zhang, H. Li, W. Xie, *Angew. Chem., Int. Ed.* **2021**, *133*, 19927.
[32] A. Bashir, J. H. Lew, S. Shukla, D. Gupta, T. Baikie, S. Chakraborty, R. Patidar, A. Bruno, S. Mhaisalkar, Z. Akhter, *Sol. Energy* **2019**, *182*, 225.
[33] C. Su, L. Zhang, Y. Han, C. Ren, Z. Yang, *Sens. Actuators, B* **2019**, *127*, 304.
[34] Z. Wang, L. Xu, F. Huang, L. Qu, J. Li, K. A. Owusu, Z. Liu, Z. Lin, B. Xiang, X. Liu, *Adv. Energy Mater.* **2019**, *9*, 1900390.
[35] H. Niu, Z. Zhang, X. Wang, X. Wan, C. Shao, Y. Guo, *Adv. Funct. Mater.* **2021**, *31*, 2008533.
[36] J. Cai, Y. Wei, A. Cao, J. Huang, Z. Jiang, S. Lu, S. Q. Zang, *Appl. Catal., B* **2022**, *316*, 121683.

[37] W. Li, J. Liu, P. Guo, H. Li, B. Fei, Y. Guo, H. Pan, D. Sun, F. Fang, R. Wu, *Adv. Energy Mater.* **2021**, *11*, 2102134.
[38] D. Chen, S. Zhang, X. Bu, R. Zhang, Q. Quan, Z. Lai, W. Wang, Y. Meng, D. Yin, S. Yip, *Nano Energy* **2022**, *98*, 107338.
[39] Y. T. Xu, M. Y. Xie, H. Zhong, Y. Cao, *ACS Catal.* **2022**, *12*, 8698.
[40] R. Daiyan, T. Tran-Phu, P. Kumar, K. Iputera, Z. Tong, J. Leverett, M. H. A. Khan, A. A. Esmailpour, A. Jalili, M. Lim, *Energy Environ. Sci.* **2021**, *14*, 3588.
[41] D. Y. Kuo, H. Paik, J. Kloppenburg, B. Faeth, K. M. Shen, D. G. Schlom, G. Hautier, J. Suntivich, *J. Am. Chem. Soc.* **2018**, *140*, 17597.
[42] S. Li, R. Ma, J. Hu, Z. Li, L. Liu, X. Wang, Y. Lu, G. E. Sterbinsky, S. Liu, L. Zheng, *Nat. Commun.* **2022**, *13*, 2916.
[43] H. Yin, Z. Chen, S. Xiong, J. Chen, C. Wang, R. Wang, Y. Kuwahara, J. Luo, H. Yamashita, Y. Peng, *Chem. Catal.* **2021**, *1*, 1088.
[44] Y. Yu, C. Wang, Y. Yu, Y. Wang, B. Zhang, *Sci. China Chem.* **2020**, *63*, 1469.
[45] R. Jia, Y. Wang, C. Wang, Y. Ling, Y. Yu, B. Zhang, *ACS Catal.* **2020**, *10*, 3533.
[46] Y. Zhang, Y. Zhao, Z. Chen, L. Wang, L. Zhou, P. Wu, F. Wang, P. Ou, *J. Electrochem. Soc.* **2018**, *165*, E420.
[47] A. O. Juma, E. A. Arbab, C. M. Muiva, L. M. Lepodise, G. T. Mola, *J. Alloys Compd.* **2017**, *723*, 866.
[48] P. Liu, E. J. Hensen, *J. Am. Chem. Soc.* **2013**, *135*, 14032.
[49] Y. Zhao, Y. Liu, Z. Zhang, Z. Mo, C. Wang, S. Gao, *Nano Energy* **2022**, *97*, 107124.
[50] J. Y. Fang, Q. Z. Zheng, Y. Y. Lou, K. M. Zhao, S. N. Hu, G. Li, S. G. Sun, *Nat. Commun.* **2022**, *13*, 7899.
[51] M. X. Jin, Y. L. Pu, Z. J. Wang, Z. Zhang, L. Zhang, A. J. Wang, J. J. Feng, *ACS Appl. Energy Mater.* **2019**, *2*, 4188.
[52] J. Hu, C. Zhang, Y. Zhang, B. Yang, Q. Qi, M. Sun, F. Zi, M. K. Leung, B. Huang, *Small* **2020**, *16*, 2002212.
[53] Y. Gu, S. Chen, J. Ren, Y. A. Jia, C. Chen, S. Komarneni, D. Yang, X. Yao, *ACS Nano* **2018**, *12*, 245.
[54] T. Ren, Z. Yu, H. Yu, K. Deng, Z. Wang, X. Li, H. Wang, L. Wang, Y. Xu, *Appl. Catal., B* **2022**, *318*, 121805.
[55] J. Pérez-Ramírez, N. López, *Nat. Catal.* **2019**, *11*, 971.
[56] A. Kulkarni, S. Siahrostami, A. Patel, J. K. Nørskov, *Chem. Rev.* **2018**, *118*, 2302.
[57] Q. Gao, H. S. Pillai, Y. Huang, S. Liu, Q. Mu, X. Han, H. Zhou, Q. He, H. Xin, H. Zhu, *Nat. Commun.* **2022**, *13*, 2338.
[58] M. Xu, Y. Zhang, H. Zhou, X. Li, Y. Zhou, X. Xu, G. Jia, G. P. Zhu, F. F. Wu, P. Gao, W. Ye, *Sci. China Mater.* **2023**, *66*, 1352.
[59] G. Kresse, J. Furthmüller, *Phys. Rev. B* **1996**, *54*, 11169.
[60] Y. Wang, X. Qin, M. Shao, *J. Catal.* **2021**, *400*, 62.
[61] V. Wang, N. Xu, J. C. Liu, G. Tang, W. T. Geng, *Comput. Phys. Commun.* **2021**, *267*, 108033.